

# Label-free Biosensing Using Hybrid Plasmonic Substrates Generated via Nanosphere Lithography

Elif Lulek, Arif E. Cetin,\* and Yavuz Nuri Ertas\*

Cite This: <https://doi.org/10.1021/acsnm.4c03945>

Read Online

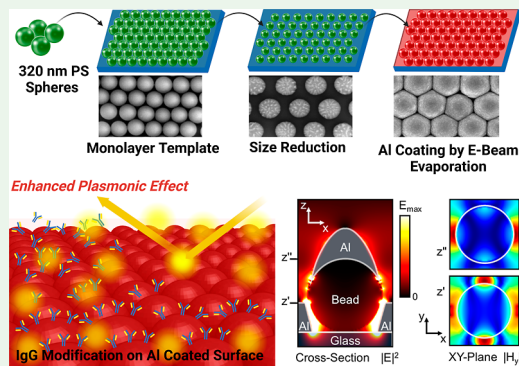
ACCESS |

Metrics &amp; More

Article Recommendations

**ABSTRACT:** The rapid advancement of air/water interface coatings transcends multiple domains. These coatings, valued for expansive coverage, facile acquisition, and economic efficiency, hold pivotal roles in nanosurface engineering. Conventional approaches to achieving 2D periodic structures, such as electron-beam lithography, suffer from cost and complexity challenges. Nanosphere lithography presents an alternative avenue by harnessing the inherent self-assembly propensity of colloidal nanoparticles and offers simplicity, cost-effectiveness, and compatibility with various techniques. The use of nanosphere lithography in coating metal templates gains traction in plasmonics because of its simplicity and speed. The fusion of plasmonics and biosensing enables label-free detection with unprecedented sensitivity, revolutionizing areas such as medicine, diagnostics, and environmental monitoring. In the realm of label-free biosensing, attaining uniform large-area fabrication is critical for robust sensing signals. Detecting spectral variations in low analyte concentrations necessitates a precise response profile. The creation of a potent and accessible local electromagnetic field is vital for enhancing light–biomolecule interactions. We introduce a hybrid plasmonic substrate via nanosphere lithography, combining antenna and aperture responses. The hybrid plasmonic design caters to the prerequisites of efficient label-free biosensing, uniform large-scale fabrication, narrow spectral response, and strong local electromagnetic fields. The hybrid plasmonic substrate promises to advance label-free biosensing capabilities by integrating antenna and aperture responses, facilitating sensitive and robust biosensing applications. Demonstrating these parameters resulted in a high refractive index sensitivity of up to 553 nm/RIU. The hybrid nature further facilitated an impressive detection limit of 0.5 ng/mL for label-free protein IgG detection.

**KEYWORDS:** nanofabrication, plasmonics, label-free biosensing, nanosphere lithography, self-assembly



## 1. INTRODUCTION

The incorporation of air/water interface coatings into various fields has seen rapid advancement in the last few decades.<sup>1</sup> Due to their properties, such as applicability to large areas, ease of acquisition, and low cost, the resultant coatings play a crucial role in the nanofabrication of surfaces.<sup>2–5</sup> The utilization of colloidal nanoparticles in coatings at the air/water interface, along with the deposition of these particles as thin films on diverse surfaces, also encompasses an important lithography technique known as colloidal lithography or nanosphere lithography.<sup>6</sup> Colloidal nanoparticles, owing to the spherical shape, arrange themselves into regularly organized, stable structures under suitable conditions to minimize Gibbs energy.<sup>7–9</sup> Due to the Marangoni effect in water, colloidal nanoparticles can form well-ordered two-dimensional (2D) structures when gradually introduced into ethanol-based solutions.<sup>10</sup> The coatings created at the air/water interface are subsequently transferred onto various surfaces, resulting in the formation of periodic 2D structures.

Various production methods can be employed to generate 2D periodic structures on diverse surfaces. These techniques encompass electron-beam lithography (EBL), block copolymer lithography, extreme-ultraviolet lithography (EUVL), capillary force-assisted lithography, fracture and cracking methods, and focused-ion beam milling.<sup>11–17</sup> Nevertheless, these methods exhibit several disadvantages. Notable factors among them include cost, installation requirements, processing time, and the limited range of designs that could be achieved. Nanosphere lithography is suggested as a solution to address these challenges. Nanosphere lithography aims to harness the capability of colloidal nanoparticles to self-arrange into a monolayer at the air/water interface, thereby creating

**Received:** July 10, 2024

**Revised:** August 14, 2024

**Accepted:** September 10, 2024

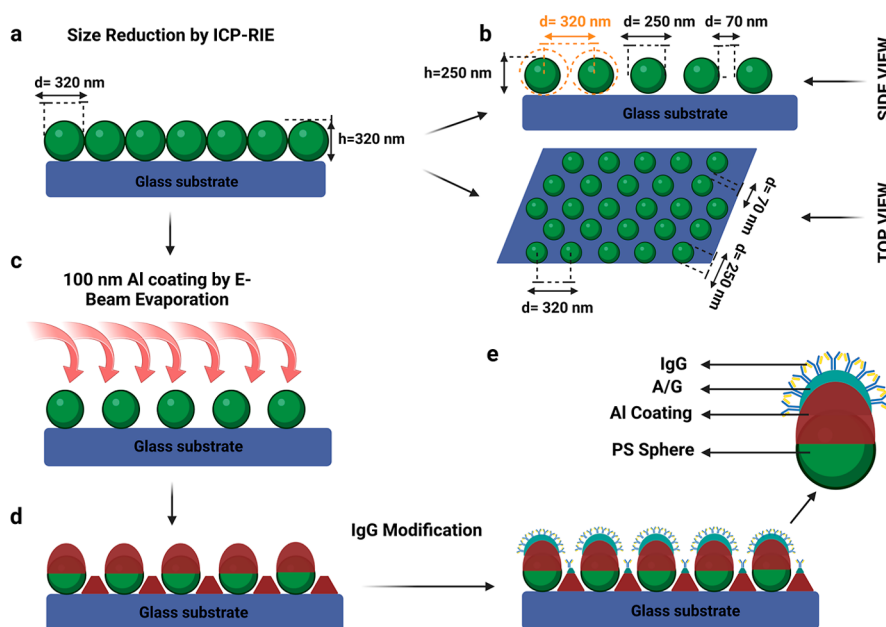


**Figure 1.** Illustration of the fabrication process. (a) Formation of a monolayer coating using polystyrene nanospheres. (b) Oxygen plasma etching for nanosphere size reduction, depicted from both top and side perspectives. Nanosphere diameters were reduced to approximately 250 nm, with gaps between adjacent nanospheres measuring  $\sim 70$  nm. (c) Subsequent to size reduction, nanospheres were coated with a 100 nm-thick layer of aluminum. (d) Side view showcasing the substrate post aluminum coating. (e) Surface modification with protein IgG, along with a detailed side view of an individual nanosphere after the modification process.

structures in a hexagonal close-packed (HCP) pattern. It offers advantages such as simplicity and cost-effectiveness in fabricating periodic 2D patterns, as well as the ability to vary the resulting patterns due to its seamless integration with various techniques.<sup>18</sup>

In recent decades, well-ordered 2D periodic structures obtained via nanosphere lithography have found numerous fields, including nanofabrication, electronics, optics, plasmonics, biosensing, and photovoltaics.<sup>2,5,19–27</sup> Coating the template structures obtained using nanosphere lithography with various metals and using them for plasmonics studies is a simple and fast method that has attracted the attention of researchers. The size of the spheres in the 2D template could be adjusted as desired, enabling homogeneous hotspots to be generated, resulting in uniform signals. A variety of applications of 2D periodic structures make plasmonics a leading edge of scientific research that has emerged as a transformative avenue in the realm of biosensing.<sup>28</sup> This fascinating field exploits the unique interactions between light and matter at the nanoscale to craft innovative sensing platforms with high precision and sensitivity.<sup>29</sup> The combination of plasmonics and biosensing could allow the detection of the smallest molecular interactions, enabling label-free detection that goes beyond traditional methods.<sup>30</sup> Using intricate nanostructures that harness the power of localized surface plasmon resonances, plasmonic biosensing has allowed us to see the subtle details of molecular binding events in real-time.<sup>31</sup> This potent amalgamation has led to the development of ultrasensitive and selective biosensors, revolutionizing fields such as medicine, environmental monitoring, and diagnostics. As plasmonic biosensing continues to evolve, it forges an exciting path toward enhanced understanding, innovative applications, and the promise of a more intricate comprehension of the biological world.

In the realm of label-free biosensing applications, several critical factors converge to define the efficacy of our approach. First, the realization of large-area fabrication characterized by exceptional uniformity holds paramount importance, as it serves as the foundation for robust sensing signals. Equally significant is the pursuit of a narrow response capability tailored to effectively track minute spectral variations even within the milieu of low analyte concentrations. Furthermore, the establishment of a substantial and easily accessible local electromagnetic field stands as a pivotal prerequisite. This dynamic field acts as a critical catalyst in generating potent sensing signals, thereby accentuating the intricate interplay between light and biological molecule interactions. The harmonious integration of these principles forms the cornerstone of our technology, positioning it as a pioneering force in advancing label-free biosensing capabilities.

In this article, we introduce a hybrid plasmonic substrate that uniquely combines plasmonic excitations stemming from both antenna and aperture responses, realized through nanosphere lithography. The hybrid plasmonic substrate addresses key requisites for efficient, label-free biosensing applications. Within such contexts, achieving large-area fabrication with uniformity becomes pivotal to engendering robust sensing signals. Equally critical is a narrow response, adept at monitoring minute spectral fluctuations, especially in the presence of low analyte concentrations. Moreover, the creation of an expansive and readily accessible local electromagnetic field proves indispensable in fostering sensing signals arising from interactions between light and biomolecules. Our hybrid plasmonic substrate employs a scalable and remarkably precise fabrication technique, centered around the development of an aperture-antenna hybrid structure. Through this inventive configuration, a fusion of antenna and aperture responses is realized, effectively inciting a plasmonic resonance associated with nanoscale optical behavior. This resonance

facilitates not only highly sensitive detection capabilities but also the generation of substantial and easily accessible electromagnetic fields. As a result, the hybrid plasmonic substrate assumes a pivotal position at the forefront of advancing label-free biosensing capabilities.

## 2. MATERIALS AND METHODS

### 2.1. Substrate Fabrication. 2.1.1. Glass Substrate Preparation.

Glass slides were procured from ISOLAB (Wertheim, Germany) and cut into square pieces measuring  $2 \times 2$  cm to function as substrate materials. These pieces were subjected to a thorough cleaning process involving organic solvents, namely acetone, ethanol, and deionized water. Each cleaning step was accompanied by a 15 min session of sonication. Following the complete cleaning procedure, the organically cleansed surfaces underwent treatment with a UV–ozone cleaner (ProCleaner Plus Bioforce Nanosciences, USA) prior to the coating procedure.

**2.1.2. Solution Preparation.** A stock solution containing 320 nm diameter carboxylated polystyrene (PS) latex nanospheres (Mag-Sphere, 10% w/v, USA) was used without dilution to prepare the solution. The coating mixture was combined with ethanol and ethylene glycol to ensure suitability for application at the air/water interface, and it was subjected to an ultrasonic bath. The solution underwent continuous sonication during the coating process to prevent any possible agglomeration. All solvents were used as received at room temperature.

**2.1.3. Monolayer Coating Process.** The prepared solution was applied onto the cleaned glass slides using an air/water interface. The clean glass slides were placed inside a glass Petri dish, and sufficient deionized water was added. The prepared PS nanosphere solution was then gradually dripped along the edge of the Petri dish. The dripped solution spread across the water surface, initiating the formation of the polymer template in a monolayer HCP arrangement. This process continued until the entire surface of the water was covered. Once the water surface was covered, the water in the Petri dish was slowly drained, allowing the PS nanosphere template to adhere to the glass slides. The covered glass slides were placed in an oven at  $60^\circ\text{C}$  for 20 min to ensure any residual water evaporated, thereby stabilizing the nanospheres on the surface. Figure 2a displays the field-emission scanning electron microscope (FESEM, Gemini 500, Zeiss, Germany) image captured after depositing the nanospheres onto the glass surfaces. Figure 3d illustrates the iridescent characteristics of the surface resulting from the application of nanospheres onto the glass surface.

**2.2. Size Reduction Process.** The PS nanospheres came into contact with each other, forming an HCP arrangement upon being coated onto the glass surfaces. The process of reducing the nanosphere size involved the use of an inductively coupled plasma-reactive ion etcher (ICP-RIE, SI 500, Sentech, Germany). Employing an oxygen plasma with an  $\text{O}_2$  flow rate of 50 sccm for 75 s, the nanosphere diameters were reduced from 320 to 250 nm. Figure 1a–d illustrate the gaps that emerged between the diminished spheres. It is presumed that the nanospheres retained their spherical geometry throughout the etching process. Following exposure to the oxygen plasma, a gap of approximately 70 nm was established between the nanospheres, as depicted in Figure 1d. Figure 2b demonstrates the reduction in nanosphere sizes while maintaining the HCP arrangement. Figure 2c illustrates the gaps that emerged between the nanospheres following their size reduction.

**2.3. Metal Coating Process.** Aluminum (Al) was selected as the target material due to its superior plasmonic properties, such as the ability to excite narrow farfield features and generate strong local electromagnetic fields. Noble metals such as silver (Ag), gold (Au), and copper (Cu) are well-known for their strong surface plasmon resonance effects, particularly in the visible to near-infrared region.<sup>32–34</sup> However, Al presents several unique advantages that make it an attractive alternative. First, aluminum is much more cost-effective due to its abundance, making it suitable for large-scale and commercial applications. Additionally, although aluminum is prone to

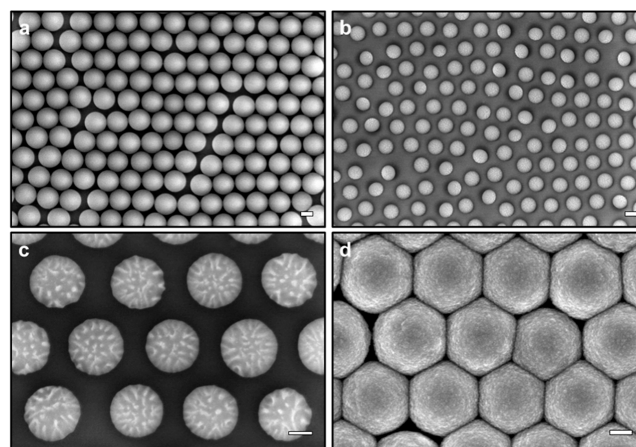


**Figure 2.** SEM images of etched nanospheres and coated surfaces. (a) Monolayer coating of polystyrene nanospheres on a glass substrate. (b) Size reduction of nanospheres after 75 s of oxygen plasma treatment. (c) Zoom-in view of (b) where the gaps between the nanospheres are  $\sim 70$  nm and diameters of nanospheres are 250 nm. (d) Nanospheres after 100 nm of Al coating. Scale bars are 200 nm in (a, b), and 100 nm in (c, d).

oxidation, the resulting oxide layer can act as a protective barrier in various environments, thereby enhancing the durability and stability of plasmonic devices. These factors make aluminum a compelling choice for our application needs.

Using an electron beam evaporator (NVTS-400, Nanovak, Türkiye), the metal coating was applied to PS nanospheres with reduced diameters. Al was deposited onto the substrates at a chamber pressure of  $10^{-6}$  torr. The coating thicknesses were determined as 25, 50, and 100 nm, with an evaporation rate of  $0.4 \text{ \AA}/\text{min}$  for all cases. To ensure uniform coating, the substrate holder rotated at a constant speed of 20 rpm. Figure 1c,d provide an illustration of the coatings formed during the application process. Figure 3a–c present the FESEM images of the coatings at various thicknesses. Figure 3d depicts the appearance of coating 320 nm nanospheres in a monolayer arrangement on glass substrates. Figure 3e displays, from left to right, the transparency characteristics of Al-coated surfaces at thicknesses of 25, 50, and 100 nm, respectively.

**2.4. Experimental Setup for the Spectral Measurements.** A comprehensive light source in the form of a broadband white light-emitting diode was employed to illuminate the plasmonic chip. The light emitted by the plasmonic substrate underwent collection through a  $100\times$  objective lens housed within an inverted microscope (Zeiss Axio Observer 7). This collected light was coupled to a multichannel spectrometer (Avantes B.V., Netherlands) using a light-coupling setup, which featured an achromatic and an objective lens with a fiber collimator. Within the multichannel spectrometer, the spectral range of interest was segmented into five individual spectrometers that functioned simultaneously. A slit width of  $5 \mu\text{m}$  was chosen to ensure a high spectral resolution of  $0.9 \text{ \AA}$ . In order to ensure reliable calculations derived from the experimental data, the transmission response of the plasmonic structure underwent a process of refinement using a Savitzky–Golay filter.

**2.5. Surface Modification for Analyte Attachment.** The bonding of analytes onto the Al surface was achieved through a process of physisorption. We followed a two-step incubation protocol for the formation of the protein bilayer consisting of proteins A/G and IgG. The initial step involved the incubation of protein A/G onto the plasmonic substrate's surface. Protein A/G attaches to the Al surface through the mechanism of physisorption. Subsequently, the protein IgG was introduced and incubated on the same surface. Protein IgG attaches to protein A/G through its Fc region. After each round of protein incubation, the chip's surface underwent a thorough rinsing procedure using both phosphate-buffered saline and DI water. This step was crucial to effectively eliminating any unbound protein

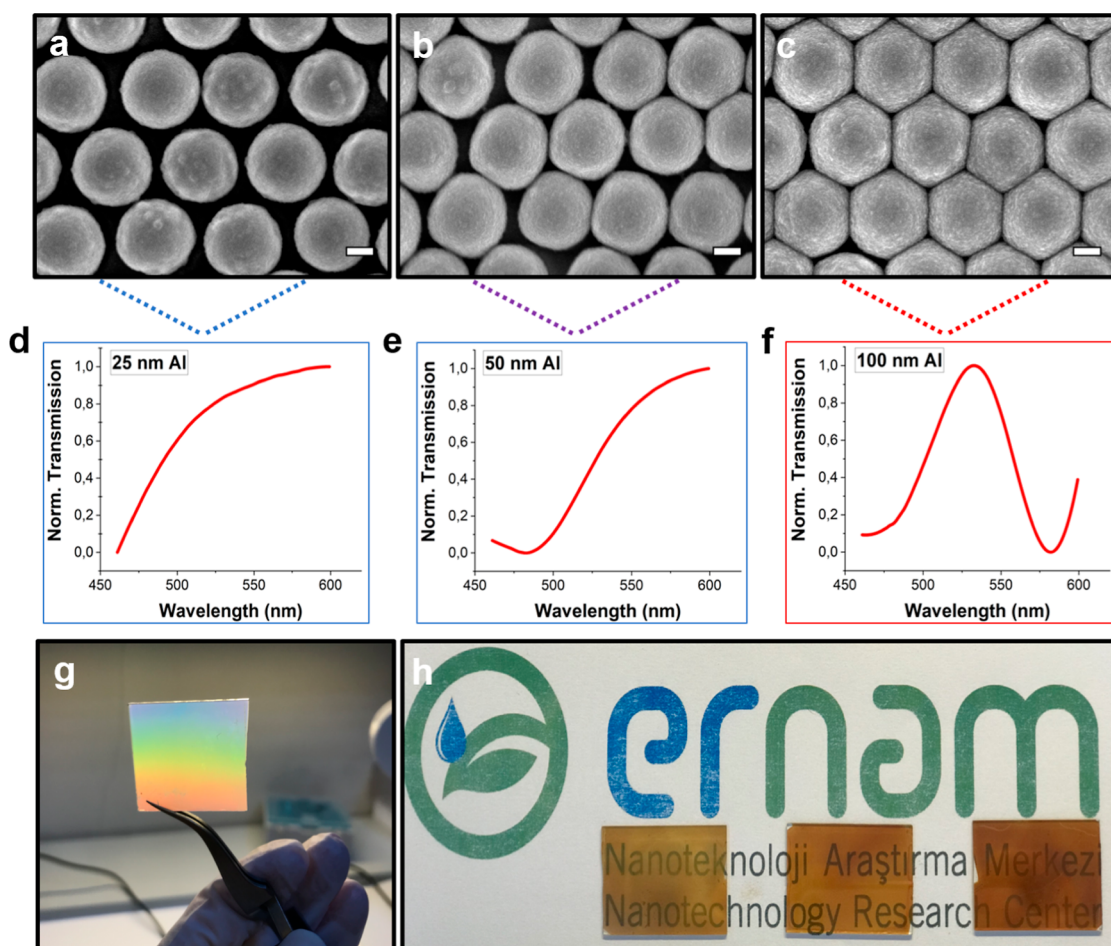


**Figure 3.** Surface behavior of size-reduced polystyrene nanospheres with varied Al coating thickness. SEM images (a–c) and transmission spectra (d–f) of Al-coated surfaces with a thickness of 25, 50, and 100 nm (Scale bars = 100 nm). (g) Iridescent behavior resulting from the Bragg diffraction effect observed on surfaces with the nanosphere template after the coating process. The iridescence is visible at varying angles of incident light. (h) Distinct transparency behaviors of surfaces with different Al coating thicknesses, from left to right: 25, 50, and 100 nm. Despite the gradual decrease in transparency with thicker coatings, the surfaces maintain appreciable transparency even after a 100 nm coating.

remnants from the surface, ensuring a well-prepared substrate for further analysis.

**2.6. Finite Difference Time Domain Simulations.** In order to elucidate the fundamental physical mechanisms governing the plasmonic resonances sustained by the Al hybrid plasmonic substrate, finite difference time domain (FDTD) simulations were executed. The simulations were conducted utilizing a unit cell encompassing a solitary particle, where periodic boundary conditions were implemented across the plane of the hybrid plasmonic substrate ( $xy$ -plane), while a perfectly matched layer boundary condition was employed along the direction of propagation ( $z$ -axis). For discretization along all directions, a mesh size of 1 nm was chosen. An  $x$ -polarized light source was employed to irradiate the plasmonic substrate.

### 3. RESULTS AND DISCUSSION

#### 3.1. Fabrication of PS Monolayer on Glass Surfaces.

The solution containing PS spheres was prepared using ethylene glycol and ethyl alcohol. The objective is to enable the application of a coating across extensive surfaces at the interface between air and water, with the goal of achieving a single layer of coating. It is critical to minimize any disruption to the template structure when transferring the monolayer template onto the substrate. In order to ensure this, PS sphere: ethyl alcohol: ethylene glycol ratios were determined as 3:3:2, respectively. These ratios were determined and refined by

iterative experimentation. A straightforward setup was made to integrate the produced solution into the air/water interface. With the aid of this homemade setup, it becomes feasible to evenly distribute the prepared solution throughout a substantial surface area while minimizing imperfections. The configuration comprises a Petri dish and a pipet. The substrate intended for coating is positioned within a Petri dish and subsequently supplemented with water. The water quantity must be adequate to facilitate the Marangoni flow, meaning that enough water should be added to fully submerge the entire substrate in the Petri dish. The prepared solution was gradually dispensed over the water surface, one drop at a time. To get optimal results, it is necessary to create a diaphragm area of the solution on the substrate precisely at the place where the drop is deposited. Consequently, the PS spheres glide across the substrate as they are put onto the water. The solution was continuously dispensed from the same location until it completely covers the entire air/water contact. In order to transfer the monolayer film structure onto the substrate, the water was gradually extracted from the edge of the Petri dish using a pipet. The Petri dish was maintained at a temperature of 60 °C for a duration of 20 min in order to eliminate any remaining liquid and facilitate the proper adhesion of the monolayer film to the substrate surface in a functional manner.

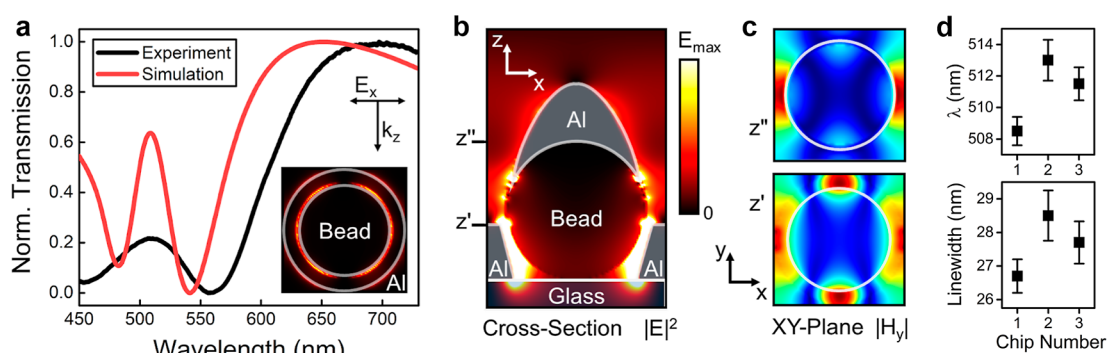


**Figure 4.** Numerical analyses of the hybrid plasmonic substrate. (a) Comparison of the experimental (black) and calculated (red) normalized transmission spectra of the hybrid plasmonic substrate. The inset in the figure illustrates the polarization and propagation direction of the incident light source, along with the electric field intensity distribution ( $|E_x|^2 + |E_y|^2 + |E_z|^2$ ) related to the transmission resonance, calculated at  $z'$ . (b) Cross-sectional profile depicting the electric field intensity supported by the plasmonic hybrid substrate. (c) Magnetic field distribution ( $|H_y|$ ) across the  $xy$ -plane, calculated at  $z'$  and  $z''$ . (d) Spectral position (top) and the line width (bottom) of the transmission resonance of three different chips. The squares correspond to the mean values and the error bars are double the standard deviation regarding the measurements from 10 separated locations with the size of  $150 \times 150 \mu\text{m}$  on each chip.

The successful formation of a monolayer structure of nanospheres at the air/water interface and the accurate transfer of this layer onto the desired substrate are two critical steps in the design of plasmonic sensors. The well-coordinated assembly of the nanospheres and the precise formation of the HCP shape enable consistent plasmonic behavior across all regions of the sensor. Achieving this uniformity depends on adjusting the surface tension of the water to ensure that the nanospheres are organized without clumping together. Ethanol was used to modify the surface tension of the water, ensuring a well-ordered 2D arrangement. Ethylene glycol was employed to prevent the agglomeration of the nanospheres and to guarantee the acquisition of the template structure over a considerable area. Additionally, room temperature was maintained to establish reproducibility and stability, and the nanosphere solution underwent frequent sonication to prevent agglomeration prior to the coating process.<sup>35</sup> Figure 1a illustrates the schematic representation of the monolayer template after its transfer onto the glass substrates. Due to the HCP film formation, the beads are in direct contact within the film structure. In Figure 2a, the formation of the monolayer and the close proximity of the beads to each other are depicted after the beads have been transferred onto the glass surfaces. The HCP form of the polymer film template significantly influences the behavior of the subsequent metal coating, which is applied in the next step to enhance plasmonic behavior. The metal coating, designed to be applied onto the film consisting of closely situated nanospheres, is deposited onto the glass substrate through the minimal gaps between the nanospheres. However, due to the increasing thickness of the coating, a thin film layer gradually forms on the nanosphere template over time. As the resultant film structure behaves like a flat surface, the generation points of “hot spots” that influence plasmonic behavior diminish, leading to a corresponding decrease in plasmonic activity. This outcome is anticipated, as the literature often notes that rough surfaces tend to generate more hot spots compared to flat surfaces.<sup>23,36</sup> This implies the need to create more space between the spheres.

**3.2. Size Reduction Process in PS Monolayer Film.** To decrease intersphere contact within the PS monolayer and enhance hot spot behavior subsequent to metal deposition, it becomes imperative to enlarge the spacing between spheres. In accordance with these requisites, oxygen plasma was

implemented to make in situ size reduction of individual nanospheres while maintaining the integrity of the HCP arrangement and the nanospheres' positional consistency. During the process of size reduction within ICP-RIE system, several critical parameters come into play: ICP power, RF power, oxygen flow, pressure, and time. To diminish the diameter of the PS nanospheres from an initial 320 nm to an average of 250 nm, the following conditions were applied: ICP power of 100 W, RF power of 50 W, and oxygen flow rate of 50 sccm for a duration of 75 s under a pressure of 75 mtorr. Each nanosphere within the template interacted with the plasma generated within the ICP-RIE setup, causing a reduction in size while preserving their relative positions, thus ensuring the HCP arrangement remained undisturbed. The in situ shrinking of individual beads without any alteration in their spatial configuration is crucial due to the nearly equidistant spacing of the spheres within the template, which is conducive to the creation of a uniform surface following the metallization process. The observed diameter of 250 nm after the beads' reduction from their initial size of 320 nm signifies an approximate average bead-to-bead distance of 70 nm. The behavior of the nanospheres as they ideally and spherically shrink onto the substrates during the etching process is illustrated in Figure 1b, showing side and top views. SEM images in Figure 2b, c further corroborate the efficacy of this process, depicting in situ shrinkage of nanospheres with near-ideal sphericity while their positions remain unaltered. Figure 2c additionally illustrates the extent to which the initially smoother surfaces of the nanospheres are transformed after exposure to oxygen plasma for the given duration.

**3.3. Metal Coating Process.** Following the fabrication of the PS template structure with dimensions defined by oxygen plasma, a metal coating procedure was executed to enhance the plasmonic characteristics of the surfaces. Electron beam evaporation was employed to deposit a metal layer onto each polymer sphere and the intersphere gaps on the substrate. Aluminum (Al) was chosen as the suitable metal for this investigation due to its stability, affordability, and notable plasmonic properties. Diverse thicknesses of Al were applied to substrates within an average pressure environment of  $10^{-6}$  torr. Substrates possessing identical PS templates were coated with varying thicknesses of Al layers (25, 50, and 100 nm), and the impact of distinct coating thicknesses on plasmonic behavior

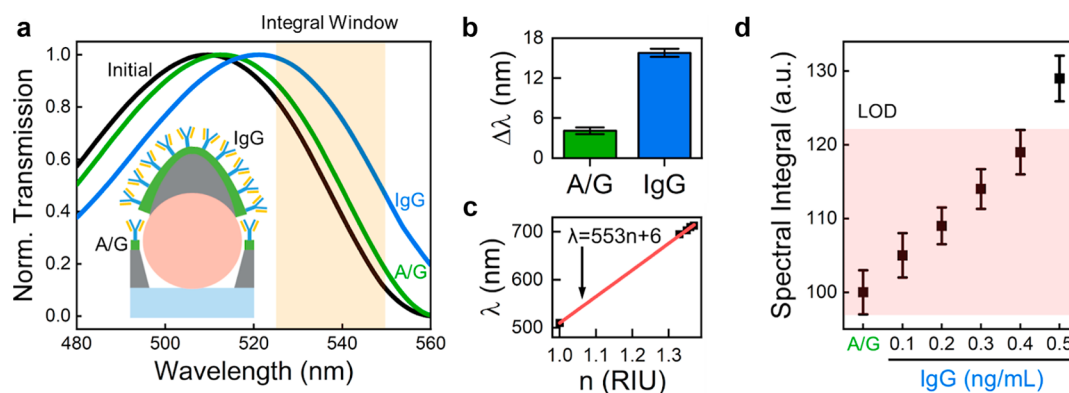


**Figure 5.** Sensing properties of the hybrid plasmonic substrate. (a) Transmission resonance of the hybrid plasmonic substrate (black) subsequent to the introduction of protein A/G (green) and protein IgG (blue). The inset in the figure schematically illustrates the proteins, showcasing the affinity of protein A/G to the Fc region of protein IgG, resulting in the IgG molecule adopting a Y-shape orientation on the surface. The spectral range where the integral calculations were conducted is highlighted in yellow. (b) Amount of the spectral shift within the transmission resonance following the functionalization of the Al surface with protein A/G (green) and protein IgG (blue). (c) Spectral position of the transmission resonance across different refractive indices of bulk solutions ( $n$ ). The red line corresponds to linear fitting applied to the experimental data (black squares). (d) Spectral integral values corresponding to 100 g/mL of protein A/G and protein IgG, encompassing concentration ranges between 0.1 ng/mL and 0.5 ng/mL. The system's limit of detection (LOD) is highlighted in red.

was observed through experimentation. SEM images of the surfaces resulting from different coating thicknesses are presented in Figure 3a–c, depicting 25, 50, and 100 nm, respectively. The graphs located above the figures illustrate the experimental outcomes of the transmission spectra associated with surfaces treated with diverse coating thicknesses. The data derived from these experiments revealed that the transmission behavior of the 100 nm Al-coated surfaces exhibited greater strength compared to the thinner coatings. In light of this finding, the subsequent stages of the experiment utilized a 100 nm Al coating, as depicted in Figure 2d, which presents the SEM image of surfaces employed for subsequent experimental measurements. It is widely recognized that the periodic arrangement of the nanosphere template yields iridescent behavior on the surface following the coating process. This phenomenon is attributed to the Bragg diffraction effect, as illustrated in Figure 3d, showing the iridescent characteristics of surfaces developed in our study. This iridescence is prominently visible from varying angles of incident light, yet it does not entirely compromise the transparency of the surfaces. Figure 3e demonstrates the distinct transparency behaviors of surfaces with varying film thicknesses (from left to right: 25, 50, and 100 nm Al coating). Thus, the metal coating process induces modifications in the template, culminating in consistent behavior throughout each region. As anticipated, transparency gradually diminished with increasing coating thickness; however, even after a 100 nm coating, the surfaces retained significant transparency properties.

**3.4. Farfield and Nearfield Properties of the Hybrid Plasmonic Substrate.** Figure 4a illustrates the transmission behavior of the hybrid plasmonic substrate as determined through visible spectroscopy (black curve) and FDTD simulations (red curve). The figure highlights that the location of the plasmonic mode aligns well between the simulation and the experimental results, indicating that our model effectively captures the essential characteristics of the fabricated structure. Here, we observed a notable difference between the simulation and the experimental response in terms of the transmission amplitude and its line width. This discrepancy can be attributed to several factors related to the structural differences between the idealized model and the actual fabricated

structures. For example, our simulations modeled the system as perfect spheres with identical metal formations, while the fabricated particles exhibit variations in size and shape, and the gaps between spheres and their periodicity slightly differentiate from each other. In Figure 4b, the cross-sectional electric field reveals a pronounced enhancement of large local electromagnetic fields concentrated within the gaps between the Al film and the beads, as well as along the edges of the Al particles. To elucidate the origin of the transmission resonance supported by the hybrid plasmonic substrate, the magnetic field distribution was examined at two positions: the top surface of the Al ( $z'$ ) and along the Al particle ( $z''$ ). As depicted in Figure 4c, the mode along the  $x$ -axis (calculated at  $z''$ ) arises from the interaction between the Al particle and the aperture along the Al film. By excluding the magnetic field distribution linked to the mode stimulated by the Al aperture-particle interaction, the remaining distribution reveals that the hot spots along the  $y$ -axis stem from localized surface plasmons. Meanwhile, the standing field pattern along the  $x$ -axis is a result of counter-propagating two surface plasmon modes. The inset of Figure 4a offers insight into the dipolar nature of the mode along the top Al surface, with local fields predominantly concentrated at the rims in alignment with the polarization direction.

In order to validate the uniformity and repeatability of our fabrication method, we conducted an evaluation on three different chips. Transmission responses were measured from 10 distinct locations with a size of  $150 \times 150 \mu\text{m}$ . Figure 4d provides a visual representation of the measured variations, showing the spectral position (top) and the line width (bottom) of the transmission resonance determined from the repetition experiment. We showed that the variation in resonance wavelength was consistently below 1.5 nm, and the line width variations were below 1 nm across all chips. These findings confirm the robustness and uniformity of our lithography-free fabrication method, enabling the production of consistent plasmonic features over large areas.

**3.5. Sensing Capabilities of the Hybrid Plasmonic Substrate.** To show the sensing potential of the hybrid plasmonic substrate, label-free biosensing experiments were conducted using protein A/G and protein IgG, wherein the

attachment of protein molecules occurred through physisorption. Notably, protein A/G contains binding domains of both protein A and protein B, exhibiting a strong affinity for the Fc region of protein IgG. Figure 5a, b present the transmission resonance and the corresponding spectral changes within the resonance in the presence of protein mono- and bilayers on the plasmonic substrate's surface. Initially located at 509.5 nm (black curve), the transmission resonance shifted to 512.46 nm (green curve) upon immobilizing 100 g/mL of protein A/G and to 521.14 nm (blue curve) with 100 g/mL of protein IgG. These significant spectral shifts could be attributed to the high refractive index sensitivity of our plasmonic substrate. Large spectral shifts in plasmonic excitations are intrinsically linked to the high refractive index sensitivity of plasmonic substrates. Plasmonic materials exhibit strong responses to changes in the local refractive index. When the refractive index around the plasmonic structure changes, it modifies the resonance conditions, resulting in a shift in the resonance wavelength. This high sensitivity occurs because plasmonic excitations are confined to the interface between the metal and the surrounding dielectric material, making them particularly responsive to environmental changes. As a result, even minor variations in the refractive index can lead to significant shifts in the transmission resonance, underscoring the high refractive index sensitivity of the plasmonic substrate. In Figure 5c, the spectral position of the transmission resonance is depicted, concerning various refractive indices of bulk solutions, such as DI-water ( $n = 1.33$ ), acetone ( $n = 1.35$ ), ethanol ( $n = 1.36$ ), and isopropanol ( $n = 1.37$ ). The figure shows the relationship between the spectral position of the transmission resonance and refractive indices. Utilizing linear fitting (red line) on the experimental data (black squares), a refractive index sensitivity ( $S = \Delta\lambda/\Delta n$ ) of 553 nm/RIU (RIU = refractive index unit) was calculated.

The robust sensitivity of our plasmonic substrate ensures a high limit of detection (LoD) capacity, which enables the detection of analytes at low concentrations. Analytes with low concentrations induce minor refractive index fluctuations, resulting in subtle spectral changes in the transmission resonance that might be challenging to discern. To enhance system sensitivity digitally, spectral variations were monitored at multiple wavelengths, generating a spectral data set accounting for collective spectral shifts. To achieve this, we calculated the integral of the transmission spectrum within an integral window (depicted as the yellow region in Figure 5a), with the window width set at 25 nm. The integral window was positioned at wavelengths larger than the transmission resonance following the addition of proteins A/G and IgG. Specifically, transmission values on the right shoulder of the transmission resonance were used for integral calculations, while the remainder was excluded. This approach mitigates the influence of the transmission resonance's spectral shape. Figure 5d illustrates the spectral integral values for protein A/G and protein IgG at concentrations ranging from 0.1 ng/mL to 0.5 ng/mL. In the figure, the black squares represent the mean of three independent experimental data sets, with error bars indicating double the standard deviation. Below 0.5 ng/mL, some of the experimental results regarding the concentrations overlap, as indicated by their standard deviations, making it difficult to reliably distinguish between these concentrations. However, the spectral integral value calculated for 0.5 ng/mL can be reliably distinguished, as it does not overlap with the spectra integral values for the lower concentrations. The red

rectangle highlights the concentrations where the spectral integral values overlap with one another. Therefore, the minimum detectable (or reliably measurable) protein concentration defining the system's limit of detection (LoD) is 0.5 ng/mL. This strong sensing capability of our hybrid plasmonic substrate holds substantial promise for various label-free biosensing applications.

#### 4. CONCLUSION

In conclusion, this study underscores the rapid progress of integrating air/water interface coatings across diverse domains, revolutionizing nanosurface engineering with their extensive coverage, easy acquisition, and economic viability. Colloidal lithography emerges as a powerful technique, leveraging self-assembling colloidal nanoparticles to achieve stable and energy-efficient arrangements. By overcoming the limitations of traditional methodologies like EBL, nanosphere lithography emerges as an effective alternative, offering simplicity, cost-effectiveness, and compatibility with various techniques. The application of well-ordered 2D structures, fabricated through nanosphere lithography, extends to fields ranging from nanofabrication to biosensing. The fusion of plasmonics and biosensing, facilitated by nanosphere lithography, introduces a transformative era of label-free detection with exceptional sensitivity. This groundbreaking approach is poised to revolutionize medicine, diagnostics, and environmental monitoring. The hybrid plasmonic substrate we introduce in this article showcases promising potential for advancing label-free biosensing capabilities. By integrating antenna and aperture responses through nanosphere lithography, we address key requirements for efficient biosensing, e.g., uniform fabrication, narrow spectral response, and enhanced local electromagnetic fields. The achieved refractive index sensitivity of 553 nm/RIU and an impressive detection limit of 0.5 ng/mL for protein IgG detection highlight the potency of our work in propelling the realm of label-free biosensing toward new horizons.

#### AUTHOR INFORMATION

##### Corresponding Authors

Arif E. Cetin – Izmir Biomedicine and Genome Center, Izmir 35340, Türkiye; Email: arifengin.cetin@ibg.edu.tr

Yavuz Nuri Ertas – Department of Biomedical Engineering, Erciyes University, Kayseri 38039, Türkiye; ERNAM – Nanotechnology Research and Application Center, Erciyes University, Kayseri 38039, Türkiye; Department of Technical Sciences, Western Caspian University, Baku AZ1001, Azerbaijan; [orcid.org/0000-0002-6791-7484](https://orcid.org/0000-0002-6791-7484); Email: yavuznuri@gmail.com

##### Author

Elif Lulek – Department of Biomedical Engineering, Erciyes University, Kayseri 38039, Türkiye; ERNAM – Nanotechnology Research and Application Center, Erciyes University, Kayseri 38039, Türkiye

Complete contact information is available at:  
<https://pubs.acs.org/10.1021/acsanm.4c03945>

##### Notes

The authors declare no competing financial interest.

## ACKNOWLEDGMENTS

This work was supported by the Erciyes University Scientific Research Projects Coordination Unit (Project No: FYG-2024-13613). Y. N. Ertas acknowledges funding support from the 2232 International Fellowship for Outstanding Researchers Program of The Scientific and Technological Research Council of Türkiye (TÜBİTAK, Project No: 118C346).

## REFERENCES

- (1) Kim, K.; Kim, B. Q.; Kim, J. Q.; Choi, S. Q. New Collapse Mechanism of Colloidal Particle Monolayers via Depletion Pressure: Formation of Large-Area Particle Multilayers at the Air–Water Interface. *J. Phys. Chem. C* **2019**, *123* (45), 27862–27867.
- (2) Lu, Y.-C.; Hsueh, C.-H. Fabrication of periodic Ag tetrahedral nanopyramids via H<sub>2</sub>O<sub>2</sub>-assisted nanosphere lithography for plasmonic applications. *Colloids Surf., A* **2021**, *628*, 127278.
- (3) Li, X.; Zhang, Y.; Li, M.; Zhao, Y.; Zhang, L.; Huang, C. Convex-meniscus-assisted self-assembly at the air/water interface to prepare a wafer-scale colloidal monolayer without overlap. *Langmuir* **2021**, *37* (1), 249–256.
- (4) Cossio, G.; Yu, E. T. Zeta potential dependent self-assembly for very large area nanosphere lithography. *Nano Lett.* **2020**, *20* (7), 5090–5096.
- (5) Liang, X.; Dong, R.; Ho, J. C. Self-assembly of colloidal spheres toward fabrication of hierarchical and periodic nanostructures for technological applications. *Adv. Mater. Technol.* **2019**, *4* (3), 1800541.
- (6) Hulteen, J. C.; Treichel, D. A.; Smith, M. T.; Duval, M. L.; Jensen, T. R.; Van Duyn, R. P. Nanosphere lithography: size-tunable silver nanoparticle and surface cluster arrays. *J. Phys. Chem. B* **1999**, *103* (19), 3854–3863.
- (7) van Dommelen, R.; Fanzio, P.; Sasso, L. Surface self-assembly of colloidal crystals for micro-and nano-patterning. *Adv. Colloid Interface Sci.* **2018**, *251*, 97–114.
- (8) Domonkos, M.; Kromka, A. Nanosphere Lithography-Based Fabrication of Spherical Nanostructures and Verification of Their Hexagonal Symmetries by Image Analysis. *Symmetry* **2022**, *14* (12), 2642.
- (9) Tao, A. R.; Huang, J.; Yang, P. Langmuir–Blodgett of nanocrystals and nanowires. *Acc. Chem. Res.* **2008**, *41* (12), 1662–1673.
- (10) Song, C.; Ye, B.; Xu, J.; Chen, J.; Shi, W.; Yu, C.; An, C.; Zhu, J.; Zhang, W. Large-Area Nanosphere Self-Assembly Monolayers for Periodic Surface Nanostructures with Ultrasensitive and Spatially Uniform SERS Sensing. *Small* **2022**, *18* (8), 2104202.
- (11) Enkrich, C.; Pérez-Willard, F.; Gerthsen, D.; Zhou, J.; Koschny, T.; Soukoulis, C. M.; Wegener, M.; Linden, S. Focused-ion-beam nanofabrication of near-infrared magnetic metamaterials. *Adv. Mater.* **2005**, *17* (21), 2547–2549.
- (12) Mojarad, N.; Kazazis, D.; Ekinci, Y. Fabrication of high aspect ratio and tilted nanostructures using extreme ultraviolet and soft x-ray interference lithography. *J. Vac. Sci. Technol. B* **2021**, *39* (4), 042601.
- (13) Osipov, A. A.; Gagaeva, A. E.; Speshilova, A. B.; Endiiarova, E. V.; Bepalova, P. G.; Osipov, A. A.; Belyanov, I. A.; Tyurikov, K. S.; Tyurikova, I. A.; Alexandrov, S. E. Development of controlled nanosphere lithography technology. *Sci. Rep.* **2023**, *13* (1), 3350.
- (14) Cai, J.; Chen, H.; Ke, Y.; Deng, S. A Capillary-Force-Assisted Transfer for Monolayer Transition-Metal-Dichalcogenide Crystals with High Utilization. *ACS Nano* **2022**, *16* (9), 15016–15025.
- (15) Pisano, F.; Balena, A.; Kashif, M. F.; Pisanello, M.; Quattieri, A.; Sileo, L.; Stomeo, T.; D’Orazio, A.; De Vittorio, M.; Pisanello, F. Plasmonic sensing with FIB-prepared 2D micro-arrays of truncated gold nano-pyramids. **2019**, arXiv preprint arXiv:1910.06398.
- (16) Huang, J.; Fan, D.; Ekinci, Y.; Padeste, C. Fabrication of ultrahigh resolution metal nanowires and nanodots through EUV interference lithography. *Microelectron. Eng.* **2015**, *141*, 32–36.
- (17) Li, R.; Li, X.; Zou, T.; Fu, W.; Xing, J.; Huang, T.; Yu, Z.; Yang, J. Deep investigation of two-dimensional structure arrays formed on Si surface. *Appl. Surf. Sci.* **2022**, *605*, 154615.
- (18) Liu, D.; Cai, W.; Marin, M.; Yin, Y.; Li, Y. Air-Liquid Interfacial Self-Assembly of Two-Dimensional Periodic Nanostructured Arrays. *ChemNanoMat* **2019**, *5* (11), 1338–1360.
- (19) Ertas, Y. N.; Jarenwattananon, N. N.; Bouchard, L.-S. Oxide-free gadolinium nanocrystals with large magnetic moments. *Chem. Mater.* **2015**, *27* (15), 5371–5376.
- (20) Li, J.; Hu, Y.; Yu, L.; Li, L.; Ji, D.; Li, L.; Hu, W.; Fuchs, H. Recent advances of nanospheres lithography in organic electronics. *Small* **2021**, *17* (28), 2100724.
- (21) Domonkos, M.; Demo, P.; Kromka, A. Nanosphere lithography for structuring polycrystalline diamond films. *Crystals* **2020**, *10* (2), 118.
- (22) Petronijevic, E.; Belardini, A.; Leahu, G.; Cesca, T.; Scian, C.; Mattei, G.; Sibilia, C. Circular dichroism in low-cost plasmonics: 2D arrays of nanoholes in silver. *Appl. Sci.* **2020**, *10* (4), 1316.
- (23) Luo, S.; Mancini, A.; Wang, F.; Liu, J.; Maier, S. A.; de Mello, J. C. High-throughput fabrication of triangular nanopag arrays for surface-enhanced Raman spectroscopy. *ACS Nano* **2022**, *16* (5), 7438–7447.
- (24) Kim, S.; Jeong, G. S.; Park, N. Y.; Choi, J.-Y. Omnidirectional and broadband antireflection effect with tapered silicon nanostructures fabricated with low-cost and large-area capable nanosphere lithography. *Micromachines* **2021**, *12* (2), 119.
- (25) Wang, W.; Qi, L. Light management with patterned micro-and nanostructure arrays for photocatalysis, photovoltaics, and optoelectronic and optical devices. *Adv. Funct. Mater.* **2019**, *29* (25), 1807275.
- (26) Erturan, A. M.; Lulek, E.; Cuhadar, S. N.; Ertas, Y. N.; Durmaz, H. Highly-sensitive detection of 2,4-dinitrotoluene using colloidal gold nanospheres. *Sens. Actuators, A* **2024**, *369*, 115091.
- (27) Ertas, Y. N.; Bouchard, L. S. Controlled nanocrystallinity in Gd nanobowls leads to magnetization of 226 emu/g. *J. Appl. Phys.* **2017**, *121* (9), 093902.
- (28) Shrivastav, A. M.; Cvelbar, U.; Abdulhalim, I. A comprehensive review on plasmonic-based biosensors used in viral diagnostics. *Commun. Biol.* **2021**, *4* (1), 70.
- (29) Minopoli, A.; Della Ventura, B.; Lenyk, B.; Gentile, F.; Tanner, J. A.; Offenhausser, A.; Mayer, D.; Velotta, R. Ultrasensitive antibody-aptamer plasmonic biosensor for malaria biomarker detection in whole blood. *Nat. Commun.* **2020**, *11* (1), 6134.
- (30) Armstrong, R. E.; Horacek, M.; Zijlstra, P. Plasmonic Assemblies for Real-Time Single-Molecule Biosensing. *Small* **2020**, *16* (52), 2003934.
- (31) Limaj, O.; Etezadi, D.; Wittenberg, N. J.; Rodrigo, D.; Yoo, D. H.; Oh, S. H.; Altug, H. Infrared Plasmonic Biosensor for Real-Time and Label-Free Monitoring of Lipid Membranes. *Nano Lett.* **2016**, *16* (2), 1502–1508.
- (32) Guan, T. F.; Liang, S. Z.; Kang, Y. C.; Pensa, E.; Li, D.; Liang, W. K.; Liang, Z. Q.; Bulut, Y.; Reck, K. A.; Xiao, T. X.; et al. High-Power Impulse Magnetron Sputter Deposition of Ag on Self-Assembled Au Nanoparticle Arrays at Low-Temperature Dewetting Conditions. *ACS Appl. Mater. Inter.* **2024**, *16* (30), 40286–40296.
- (33) Liang, S. Z.; Guan, T. F.; Yin, S. S.; Krois, E.; Chen, W.; Everett, C. R.; Drewes, J.; Strunskus, T.; Gensch, M.; Rubeck, J.; et al. Template-Induced Growth of Sputter-Deposited Gold Nanoparticles on Ordered Porous TiO<sub>2</sub> Thin Films for Surface-Enhanced Raman Scattering Sensors. *ACS Appl. Nano Mater.* **2022**, *5* (5), 7492–7501.
- (34) Schwartzkopf, M.; Rothkirch, A.; Carstens, N.; Chen, Q.; Strunskus, T.; Löhner, F. C.; Xia, S. L.; Rosemann, C.; Bießmann, L.; Körtgens, V.; et al. In Situ Monitoring of Scale Effects on Phase Selection and Plasmonic Shifts during the Growth of AgCu Alloy Nanostructures for Anticounterfeiting Applications. *ACS Appl. Nano Mater.* **2022**, *5* (3), 3832–3842.
- (35) Lulek, E.; Ertas, Y. N. Simple and Rapid Monolayer Self-Assembly of Nanoparticles at the Air/Water Interface. *Langmuir* **2024**, *40* (34), 18039–18048.
- (36) Chirumamilla, M.; Toma, A.; Gopalakrishnan, A.; Das, G.; Zaccaria, R. P.; Krahne, R.; Rondanina, E.; Leoncini, M.; Liberale, C.; De Angelis, F.; Di Fabrizio, E. 3D Nanostar Dimers with a Sub-10-nm

Gap for Single-/Few- Molecule Surface-Enhanced Raman Scattering.  
*Adv. Mater.* **2014**, *26* (15), 2353–2358.